





Irregular dependence on Stokes number, and nonergodic transport, of heavy inertial particles in steady laminar flows

Anu V. S. Nath ^{*} and Anubhab Roy [†]

Department of Applied Mechanics, Indian Institute of Technology Madras, Chennai 600036, India

S. Ravichandran [‡]

*Nordita, KTH Royal Institute of Technology and Stockholm University, Stockholm SE-10691, Sweden
and Interdisciplinary Programme in Climate Studies, Indian Institute of Technology Bombay,
Mumbai 400076, India*

Rama Govindarajan [§]

*International Centre for Theoretical Sciences, Tata Institute of Fundamental Research,
Bengaluru 560089, India*



(Received 19 April 2023; accepted 8 December 2023; published 9 January 2024)

Small heavy particles in a fluid flow respond to the flow on a timescale proportional to their inertia or Stokes number St . Their behavior has been thought to be gradually modified as St increases. We show, on the other hand, in the steady spatially periodic laminar Taylor-Green vortex flow, that particle dynamics, and their effective diffusivity, actually change in an irregular, nonmonotonic, and sometimes discontinuous manner with increasing St . At $St \sim 1$, we show chaotic particle motion, contrasting with earlier conclusions for heavy particles in the same flow [Wang *et al.*, *Phys. Fluids* **4**, 1789 (1992)]. Particles may display trapped orbits, or unbounded diffusive or ballistic dispersion, with the vortices behaving like scatterers in a soft Lorentz gas [Klages *et al.*, *Phys. Rev. Lett.* **122**, 064102 (2019)]. The dynamics is nonergodic.

DOI: [10.1103/PhysRevFluids.9.014302](https://doi.org/10.1103/PhysRevFluids.9.014302)

I. INTRODUCTION

Particle-laden fluid flows are common in natural and industrial settings. While sufficiently small particles follow fluid streamlines, finite-sized inertial particles generally do not. The dynamics of small spherical particles of density ρ_p asymptotically greater than the density ρ_f of the ambient fluid is described by the Maxey-Riley equation [1] in its simplest nondimensional form:

$$\dot{\mathbf{x}} = \frac{\mathbf{u}(\mathbf{x}) - \mathbf{v}}{St} \quad \text{with} \quad \dot{\mathbf{x}} = \mathbf{v}, \quad (1)$$

where \mathbf{v} is the Lagrangian velocity of the particle, \mathbf{u} is the fluid velocity at the instantaneous particle location \mathbf{x} , and the overdot a derivative in time. The Stokes number St is a measure of the particle inertia and is defined as the ratio of the particle relaxation timescale $\tau_p = (2a^2\rho_p/9\nu\rho_f)$ to the fluid

^{*}am18d701@smail.iitm.ac.in

[†]anubhab@iitm.ac.in

[‡]sravichandran@iitb.ac.in

[§]rama@icts.res.in

timescale τ_f ; where a is the radius of the particle and ν is the kinematic viscosity of the ambient fluid.

Cellular flows—flows that consist of multiple adjoining closed vortical regions—are encountered in various physical contexts. For example, in the case of extensional rheological studies, experiments have been performed in four-roll mills [2,3], which generate a representative basic vortex cell of the Taylor-Green (TG) vortex flow. Microfluidic versions of four-roll mills also be found in recent experimental studies [4,5]. The flow field generated by the four-roll mill constitutes a finite version of the TG flow field without periodic repetition. However, the periodic array of TG vortex has also been used in the experiments and theoretical modeling of tiny particles like plankton suspension in Langmuir circulation [6,7] or sedimentation of fibres in similar flowfield [8]. Moreover, the Rayleigh-Benard convection cells resemble the infinite periodic array of TG vortices, modeled and studied similarly [9,10]. The Taylor-Green vortex flow, providing a time-independent spatially periodic laminar background flow, has been used to study inertial particle dynamics, e.g., by Wang *et al.* [11] who find particle motion (in the absence of gravity) to be regular when $StR \leq 1$ and chaotic when $StR \geq 1$, where $R \equiv \rho_f/(\rho_p + \rho_f/2)$ quantifies the density ratio between particle and ambient fluid. In particular, they report purely periodic particle dynamics in the heavy particle limit ($R = 0$). Wang *et al.* [11] focus on particles with finite density ratios (R) and report (1) that the large-time Lyapunov exponents of the system are distributed unimodally and, therefore, (2) that the large-time Lyapunov exponents are independent of initial conditions (ICs) for any St . In the limit $R \rightarrow 0$, their limited results pertain only to large Stokes numbers $St \gtrsim 3$, and thus they report only periodic dynamics and open trajectories for heavy particles.

Here we study the dispersion and dynamics of heavy ($R = 0$) inertial particles in TG vortex flow. We find that the behavior is highly sensitive to ICs and Stokes number (when $St \sim 1$), and remarkably, that the dependence on Stokes number is highly irregular. The transport over large ranges of St is nonergodic, i.e., dependent on the initial particle location. Certain ranges of St support multiple types of particle trajectories (open vs closed, and trapped vs diffusive vs ballistic), and the fraction of initial locations from where particles display each is a sensitive function of St . We also find small windows in St where the display of such multiple behaviors collapses abruptly and where the sudden appearance or disappearance of certain behaviors occurs. In contrast to Wang *et al.* [11], we show that heavy particles ($R = 0$) of $St \sim 1$ can display chaotic dynamics. We show that the periodicity of the TG vortex field is responsible for the dynamical richness observed. The sensitivity of the dynamics to the Stokes number manifests itself in the existence of fractal “basins of behavior,” as we shall see, whose areas are proportional to the fraction of particles that will display a given behavior. Similar fractal basins of attraction are, for example, also observed in the context of periodically driven nonlinear damped pendulum [12] or a magnetic pendulum [13]. These systems are fundamentally nonlinear oscillators excited periodically in time. However, the time dependence of the “forcing” in our system is implicit [see Eq. (2)] and arises through mutual nonlinear coupling. Our system may be transformed into a form similar to that of the “Chirikov standard map,” where deterministic diffusion and fractal transport coefficients have been extensively studied [14]. The discrete Chirikov standard map shows periodic, quasiperiodic, and chaotic dynamics depending on the initial condition [15,16].

Relevant to fluid mechanics context, Lagrangian chaos can never occur in two-dimensional (2D) steady flows; however, fluid flow around a periodic array of obstacles or stagnation points (SPs) is known to induce anomalous (sub-, and super-) diffusion of passive tracers [17–19], due to singularities of passage times near the obstacles or SPs. Continuous dynamical systems, such as the transport of tracers in deterministic time-periodic or three-dimensional flows, can be chaotic [20], but not in 2D steady deterministic flows (like ours). Though our system contains a periodic array of SPs, which brings similarity to the system described in [18], the finite inertia of our particles makes the physics different here. In our system, the regular and chaotic dynamics emerge from the interplay of particle inertia and the existence of SPs. Qualitatively diverse trajectories are known to exist in systems unrelated to fluid mechanics as well (e.g., [21–24]). The Hamiltonian system in [21] displays ballistic, trapped, and diffusive trajectories, where the effective diffusivity shows fractal

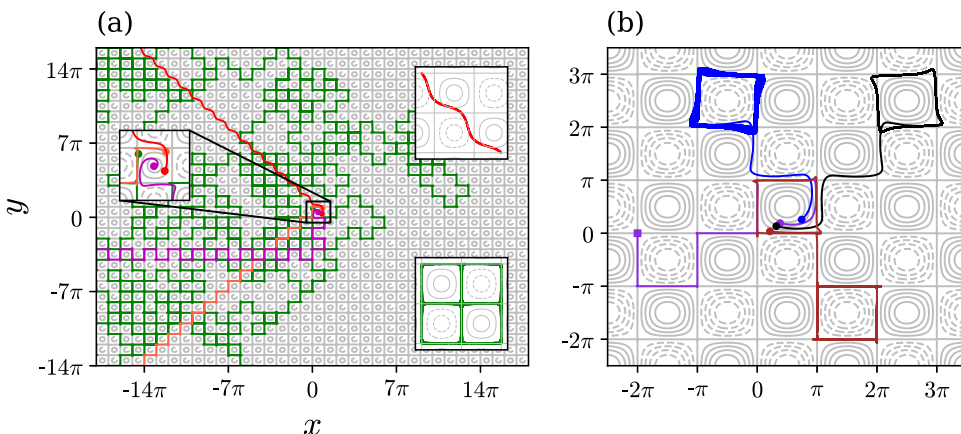


FIG. 1. Typical particle trajectories exhibiting ballistic, diffusive, and trapped dynamics. The thin gray lines are streamlines of the TG vortex flow. (a) Particles initialized at (i) (0.12,2.6) with $St = 1.12$ (green, diffusive), (ii) (2.6,2.8) with $St = 0.95$ (orange, diagonal “square ballistic”), (iii) (2.48,1.07) with $St = 1.83$ (red, diagonal smooth ballistic), and (iv) (1.5,1.5) with $St = 1.133$ (magenta, horizontal ballistic). The (left) zoomed inset shows the initial positions by filled circles. The other insets (right) show the ballistic (smooth) and diffusive trajectories in compactified physical space. (b) Particles initialized at (i) (1.0,0.42) with $St = 1.12$ (black, limit cycle), (ii) (2.33,0.81) with $St = 1.37$ (blue, chaotic attractor), (iii) (0.664,0.11) with $St = 0.89$ (brown, trapped in square limit cycle), and (iv) (1.2,0.6) with $St = 0.5$ (violet, trapped at the SP shown by the filled square). All trajectories plotted conserve the quantity Q to better than 0.1%, as shown in Fig. 12 in Appendix A.

dependence on the control parameter (energy). In comparison, our system does not have a constant Hamiltonian (see Sec. II). Nevertheless, we do observe such trajectories (Fig. 1) and, moreover, a fractal dependence of effective diffusivity with control parameter Stokes number [inset in Fig. 9(a)]. The dynamics of inertial particles in a TG vortex flow resemble a soft Lorentz gas [25] with inertial particles being “scattered” by the vortices while navigating the SPs. It is instructive to briefly discuss the soft Lorentz gas model here, which is based on the motion of point particles in a periodic lattice of partially overlapping Fermi potentials and is used to describe the dynamics of electrons in graphene-like structures. Simulations suggest that the particles can have closed or open periodic trajectories, with the latter displaying super-diffusive dynamics. Moreover, the diffusive parameter is found to have a fractal dependence on the control parameter (spacing between scattering centers). By analogy, the TG vortex flow has an infinite array of vortices and SPs arranged in a periodic lattice, with the Stokes number of the particles as the control parameter. As we shall see, closed and open periodic trajectories are observed here too.

The remainder of this paper is organized as follows. In Sec. II we set down the mathematical formulation used in this study. Methods used to distinguish the particle dynamics are listed in Sec. III. The central results are consolidated and discussed in Sec. IV. We conclude in Sec. V.

II. MATHEMATICAL MODEL

The dynamical equations for a heavy inertial particle in a two-dimensional, steady, Taylor-Green (TG) vortex flow of stream function $\psi = \sin x \sin y$ can be written from Eq. (1) as

$$\dot{x} = v_x, \quad \dot{v}_x = \frac{-v_x + \sin x \cos y}{St}, \quad (2a)$$

$$\dot{y} = v_y, \quad \dot{v}_y = \frac{-v_y - \sin y \cos x}{St}, \quad (2b)$$

where the dynamical variables (x, y) and (v_x, v_y) represent the positions and velocities of the particle, respectively, constituting a four-dimensional phase space. The system represents two coupled damped oscillators. The coupling is nonlinear, leading to the complex dynamics discussed in this paper. The system can be written in the simple symmetrical form in the rotated coordinates $z = x + y$, $w = x - y$, $\dot{z} = v_x + v_y$ and $\dot{w} = v_x - v_y$ as

$$\text{St} \ddot{z} + \dot{z} = \sin w, \quad (3a)$$

$$\text{St} \ddot{w} + \dot{w} = \sin z. \quad (3b)$$

This apparently simple system, equivalent to two coupled damped oscillators with nonlinear, periodic forcing, can nevertheless produce complicated dynamics, as we shall see. Due to the nonlinear terms and mutual coupling, these equations are impossible to solve analytically. A formal solution of Eqs. (2) in terms of (coupled) integral equations may be written down, as

$$x(t) = x(0) + \int_0^t \left[v_x(0) + \frac{1}{\text{St}} \int_0^{t'} e^{t''/\text{St}} \sin x(t'') \cos y(t'') dt'' \right] e^{-t'/\text{St}} dt', \quad (4a)$$

$$y(t) = y(0) + \int_0^t \left[v_y(0) - \frac{1}{\text{St}} \int_0^{t'} e^{t''/\text{St}} \sin y(t'') \cos x(t'') dt'' \right] e^{-t'/\text{St}} dt'. \quad (4b)$$

Here $(x(0), y(0))$ and $(v_x(0), v_y(0))$ are initial positions and velocities of the particle respectively. Thus, the particle dynamics is specified given its initial position, initial velocity, and the Stokes number. From the form of Eqs. (4), one can show that both $x(t)$ and $y(t)$ are in general unbounded quantities. However, the velocities $v_x(t)$ and $v_y(t)$ always will be bounded, with $|v_x(t)| < 1$ and $|v_y(t)| < 1$.

The dynamical equations (2) can be obtained from a corresponding Lagrangian $\mathcal{L} = (T - V)e^{t/\text{St}}$, where $T = (\dot{x}^2 - \dot{y}^2)\text{St}/2$ and $V = \cos x \cos y$, equivalent to the kinetic and potential energy, respectively. Here the time dependency of Lagrangian is a result of dissipation in the system, similar to a damped pendulum case [26]. A Legendre transformation yields the time-dependent Hamiltonian $\mathcal{H}(t) = e^{-t/\text{St}} (p_x^2 - p_y^2)/(2\text{St}) + e^{t/\text{St}} \cos x \cos y = (T + V)e^{t/\text{St}}$, where the canonical momenta are related to the velocity as $p_x = \dot{x} \text{St} e^{t/\text{St}}$ and $p_y = -\dot{y} \text{St} e^{t/\text{St}}$. Since the Hamiltonian is explicitly dependent on time, it cannot be a conserved quantity. Interestingly, the quantity $\mathcal{Q} = T + V + \frac{2}{\text{St}} \int_0^t T dt$ is a constant of our dynamics, which can be verified by taking the time derivative and showing $\dot{\mathcal{Q}} = 0$. We use this fact to check the accuracy of all our numerical simulations (cf. Fig. 1 and Appendix A). We may also relate Eqs. (2) or (3) to Bateman's time-independent Hamiltonian for dissipative systems [27] where the dual system would correspond to dynamics of inertial particles experiencing "negative" drag. As Bateman points out, since our system is dissipative, we can consider a dual or complementary system all along such that the full system now will have a time-independent Hamiltonian. If we consider Eqs. (3) along with the dual system

$$\text{St} \ddot{\zeta} - \dot{\zeta} = \gamma \xi \cos z, \quad (5a)$$

$$\text{St} \ddot{\xi} - \dot{\xi} = \gamma^{-1} \zeta \cos w, \quad (5b)$$

then the Lagrangian of the full system can be obtained using Bateman's method as

$$\mathcal{L}_f = \text{St} \dot{z} \dot{\zeta} + (-\dot{z} + \sin w) \zeta + \gamma [\text{St} \dot{w} \dot{\xi} + (-\dot{w} + \sin z) \xi], \quad (6)$$

where $(\zeta, \xi, \dot{\zeta}, \dot{\xi})$ are the dual variables to (z, w, \dot{z}, \dot{w}) , and γ is some arbitrary nonzero number. Note that the dual system has "negative" damping, which, along with the original system, makes a nondissipative full system. Though the original system can be independent of the dual system, the dual system has forcing terms which couple it back to the original system. Using a Legendre

transformation, we can obtain the equivalent Hamiltonian of the extended system as

$$\mathcal{H}_f = \frac{(\zeta + p_z)p_\zeta + (\xi + \gamma^{-1} p_w)p_\xi}{\text{St}} - (\zeta \sin w + \gamma \xi \sin z), \quad (7)$$

where the generalized coordinates (z, w, ζ, ξ) and velocity $(\dot{z}, \dot{w}, \dot{\zeta}, \dot{\xi})$ of the full system are related to the corresponding momenta $(p_z, p_w, p_\zeta, p_\xi)$ as $p_z = (-\zeta + \text{St} \dot{\zeta})$, $p_w = \gamma(-\xi + \text{St} \dot{\xi})$, $p_\zeta = \text{St} \dot{z}$, and $p_\xi = \gamma \text{St} \dot{w}$.

The form of the solution, along with sinusoidal velocity components in Eqs. (4), is tedious to track analytically. Thus, we adopt numerical methods to solve Eqs. (2) as discussed below. However, it is possible to construct a synthetic flowfield that qualitatively mimics TG vortex flow, for which the solutions can be obtained analytically—the discussion of which we defer until Sec. IV D.

A cloud of noninteracting particles is initialized within a “basic vortex cell” (exploiting the spatial symmetry of the TG vortex flowfield) of dimensions $\pi \times \pi$, consisting of a central vortex with four SPs at its corners and bounded by separatrices $x = 0$, $x = \pi$, $y = 0$, and $y = \pi$. For each Stokes number, we initialize 10 000 particles (unless specified otherwise) uniformly in the basic vortex cell and track each particle in time by integrating Eqs. (2) using a Runge-Kutta scheme of fourth-order accuracy. The size of the time step was chosen in each case so as to preserve the constant of dynamics \mathcal{Q} upto a maximum percentage error of 0.1%, (see Appendix A). The initial velocity of all particles is set to zero, and we have verified that a different choice does not alter the dynamics qualitatively (see Sec. IV C). Once a particle leaves the original basic vortex cell, it enters an identical neighboring cell, and we continue to track it in the Lagrangian sense. We continue this tracking even if the particle travels very far from the cell it has started in, by extending the domain to as big a one as needed (as we see later, that is the case with certain particles like diffusive and ballistic ones). We do not delete a particle or impose any periodicity on its leaving and entering. Instead, particles sample an unbounded domain of identical TG vortex arrays. We classify trajectories as trapped, diffusive, or ballistic according to their dispersion in the large time limit (i.e., after 10^3 – 10^4 time units) using, e.g., the squared displacement (SD) and mean characteristic speed (see Secs. III A and III B). We also classify trajectories according to their dynamical nature using tools like Lyapunov exponents, autocorrelation, and frequency spectrum (see Secs. III C, III E, and III F). Since we are interested in both the dispersion as well as the chaotic or nonchaotic nature of trajectories, we henceforth use “dispersion” to refer to the trapped, diffusive or ballistic nature of particle trajectories and “dynamics” to refer to regular or chaotic dynamical nature of trajectories.

III. METHODS

For small Stokes numbers St , after the initial stage in which particles get centrifuged out of the central vortex (e.g., [28–30]), the dynamics is primarily confined along separatrices and SPs. Particles with $\text{St} < 1/4$ remain confined within the vortex cell (by the separatrices) where they are initialized, whereas particles with higher Stokes can leak through to neighboring cells. Linear stability analysis (e.g., [29,31,32]; see also [33]) yields the critical value $\text{St} = 1/4$. For $1/4 < \text{St} \lesssim 0.77$, we find that particles leave their initial cell but get trapped at the SPs of neighboring cells. Formally, SPs have stable and unstable eigenvalues (saddle type). In our simulations, however, we see the particles getting trapped at them. This observation may be explained by noting that the velocities of particles decrease exponentially (as they must) as they get closer to SPs along the stable manifolds [34,35]. When $\text{St} \gtrsim 0.77$, we find bounded and unbounded particle trajectories that may be regular or chaotic, depending on St and initial particle position $[x(0), y(0)]$. We note that the value 0.77 is numerically obtained and is not presently analytically justified. Typical unbounded and bounded trajectories in physical space x vs y are plotted in Figs. 1(a) and 1(b), respectively. As seen in the figure, these trajectories can be regular or chaotic. Trajectories in compactified physical space, shown in the insets on the right in Fig. 1(a) (see also Sec. III D), highlight the difference between regular trajectories, which are simple curves, and chaotic trajectories, which are space-filling (especially close to SPs), indicating strange attractors.

We note that the smoothness and the boundedness of trajectories are independent properties: we find unbounded ballistic trajectories that are smooth (e.g., for $St \sim 2$) or “square” (for $St \sim 1$), respectively, shown in red and orange in Fig. 1(a). Similar smooth “zig-zag”-type trajectories were also observed in the ballistic settling of inertial particles under gravity in the TG vortex [36,37]. Analogously, we see different kinds of bounded trajectories in Fig. 1(b), where representative particle trajectories asymptote to limit cycles, SPs, and strange chaotic attractors. Limit cycles form a simple closed curve, while the chaotic trapped trajectories fill a certain region around the separatrices without ever repeating the winding.

Figure 1(a) also shows the existence of trajectories that resemble random walks (Green curve). The particle diffusivity along such trajectories is generally a function of the particle residence time in the vicinity of SPs [18].

As stated in Sec. II, we classify particle trajectories based on their large-time dispersion into trapped, diffusive, or ballistic types. We also classify them according to their large-time dynamical behavior as regular or chaotic. The metrics used to quantify these properties are discussed next.

A. Squared displacement (SD)

The dispersion of a particular particle can be measured in terms of its squared displacement [SD, denoted as $\sigma^2(t)$] from its initial location, defined as

$$\sigma^2(t) = \|\mathbf{x}(t) - \mathbf{x}(0)\|^2 = [x(t) - x(0)]^2 + [y(t) - y(0)]^2, \quad (8)$$

where $\|\cdot\|$ is the Euclidean norm. The behavior of the SD is analyzed for each trajectory at its large-time limit. If in the large-time limit, SD scales with time as $\sigma^2(t) \sim t^\alpha$, then depending on the value of α , particle trajectories may be classified as ballistic ($\alpha = 2$), diffusive ($\alpha = 1$), or trapped ($\alpha = 0$). The typical SD curves for a $St = 1.18$ particles showing each of these dynamics can be found in Fig. 8(b).

Unlike for ballistic or trapped trajectories, α is poorly defined for individual diffusive trajectories given their (deterministic-) chaotic nature, and we find values different from 1. Usually, in stochastic or random-walk situations, ensemble or time averages of the trajectories need to be taken to make the data smooth enough. Then finding the scaling of SD with time will become easier. We, therefore, use the time-averaged mean square displacement (TAMSD) (see [38]) defined as

$$\delta^2(\Delta) = \frac{1}{T - \Delta} \int_0^{T-\Delta} \|\mathbf{x}(t' + \Delta) - \mathbf{x}(t')\|^2 dt', \quad (9)$$

where Δ is the “lag time” and T is the maximum time up to which the data are available and simulation is performed. The exponent α can then be obtained from $\delta^2(\Delta) \sim \Delta^\alpha$ for individual trajectories, as the slope of the linear fit between $\log(\delta^2)$ and $\log(\Delta)$. Note that $1 \ll \Delta_{\max} \ll T$ is required for reliable statistics. Since $T = 10^4$ in our simulations, we restrict $\Delta_{\max} = 300$ to evaluate α in, e.g., Fig. 2(a).

For illustration, the value of α for all particles with $St = 1.18$ initialized within the basic vortex cell is plotted as a histogram in Fig. 2(a). The histogram shows multimodality and segregates the trapped, diffusive, and ballistic particles. All the ballistic particles acquire a directed motion quickly along definite directions, ensuring a narrow distribution of α around 2 in the figure. Trapped particles also have definite motion towards particular limit cycles, which differ from case to case. The final trajectories could be limit cycles or chaotic attractors. Moreover, the broad distribution of α around zero in Fig. 2(a) may have contributions from the error associated with the evaluation of the slope of $\log(\delta^2)$ line with $\log(\Delta)$. This error is due to the small mean value and larger oscillations of δ^2 of trapped trajectories compared to ballistic trajectories, which reduces the accuracy of the linear fit. In the case of diffusive particles, the randomness in each of the trajectories brings a distribution of α values around the mean 1, as seen in the figure.

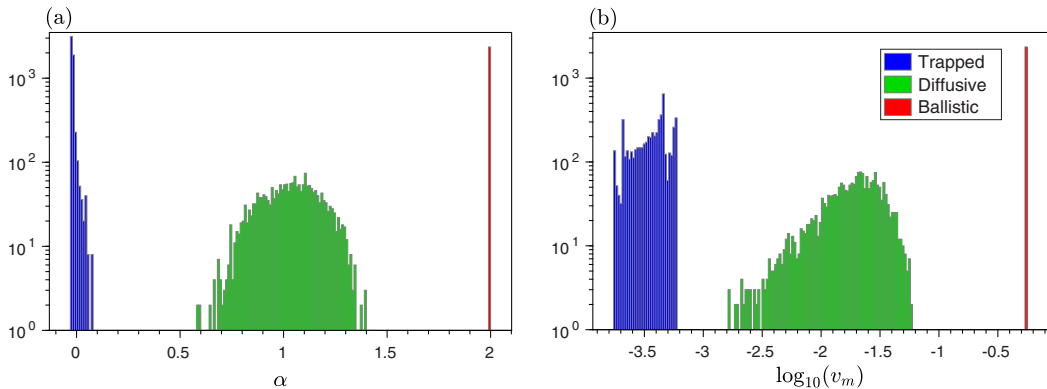


FIG. 2. Trapped, diffusive, and ballistic particle trajectories at the same Stokes number $St = 1.18$ have distinct signatures. Histograms of the number of trajectories vs (a) α and (b) the mean characteristic speed $\log_{10}(v_m)$ defined in Secs. III A and III B are shown respectively. A total of 100×100 trajectories are integrated until $T = 10^4$ and grouped using a bin size of 10^{-2} . The standard color scheme of blue: trapped, green: diffusive, and red: ballistic is used.

B. Mean characteristic speed

We define the mean characteristic speed of a particle as

$$v_m = \|\overline{\mathbf{v}(t)}\| = \sqrt{\overline{v_x(t)^2} + \overline{v_y(t)^2}}, \quad (10)$$

where $\overline{(\cdot)}$ denotes the time average over the large time limit, where the dynamics is stationary [typically in the range $t \in (10^3, 10^4)$]. Note that this is not the RMS velocity $\sqrt{\overline{v_x^2} + \overline{v_y^2}}$, nor is it the mean speed $\overline{\sqrt{v_x^2 + v_y^2}}$, which would be nonzero for both ballistic and diffusive trajectories and thus would not distinguish between these. Instead, our definition of v_m may be used to distinguish between ballistic and diffusive trajectories: ballistic trajectories have nonzero v_m , and diffusive trajectories have zero v_m , as evidenced in Fig. 2(b).

For ballistic particles, v_m will be a finite $O(1)$ value. However, it will decay to zero for trapped particles, and diffusive particles as the T becomes large enough. However, this decay will be faster for trapped particles than for diffusive ones, as shown in the histogram of values in Fig. 2(b). Distinct clusters in the histogram distinguish trapped, diffusive, and ballistic particle trajectories in the ascending order of v_m . We see that ballistic and trapped particles have narrowly distributed mean velocities (noting that the apparent broadness of the distribution for trapped particles is an artifact of the logarithmic scale used). By contrast, diffusive particles show a broad distribution of v_m .

C. Large-time Lyapunov exponents

The mean characteristic speed and squared displacement defined above may be used to distinguish between ballistic, diffusive, and trapped trajectories. Each of these trajectories may, in addition, be regular or chaotic, which may be identified using large-time Lyapunov exponents. A detailed discussion on the theory of Lyapunov exponents can be found in [39–42]. For completeness, some relevant aspects are included here as well.

In a phase space, if all points in the neighbourhood of a trajectory converge toward the same orbit, that attractor is a fixed point or a limit cycle. However, if the attractor is strange, trajectories that start sufficiently close separate exponentially with time. In a finite time, their separation attains the size of the accessible phase space. This sensitivity to initial conditions can be quantified in terms of the largest Lyapunov exponent, λ_1 , which thus measures the mean rate of separation of trajectories

of the system:

$$\delta(t) \approx \delta(0) e^{\lambda_1 t} \Rightarrow \lambda_1 = \lim_{t \rightarrow \infty} \frac{1}{t} \ln \frac{\|\delta(t)\|}{\|\delta(0)\|}, \quad (11)$$

where the initial separation between the trajectories $\delta(0)$ and the final separation $\delta(t)$ should be asymptotically small. Similarly, the mean rate of growth or contraction of a small area between three nearby trajectories in phase space is $\lambda_1 + \lambda_2$, where λ_2 is the second largest Lyapunov exponent; the mean rate of growth or contraction of small volume between four nearby trajectories in phase space is $\lambda_1 + \lambda_2 + \lambda_3$, where λ_3 is the third largest Lyapunov exponent, and so forth. In general, for a system with N phase space dimensions, there will be N Lyapunov exponents forming the Lyapunov spectrum $(\lambda_1, \lambda_2, \dots, \lambda_{N-1}, \lambda_N)$ with $\lambda_1 \geq \lambda_2 \geq \dots \geq \lambda_{N-1} \geq \lambda_N$. The sum of all Lyapunov exponents measures the growth or contraction rate of volumes in phase space. In dissipative systems, the sum is negative, meaning that volumes visited by generic trajectories shrink exponentially to zero. However, in Hamiltonian systems, they sum to zero, and thus the phase space volume is preserved by Liouville's theorem [43].

For a general autonomous dynamical system $\dot{\mathbf{x}} = \mathbf{F}(\mathbf{x})$, and a given trajectory $\mathbf{x}(t)$, the deformation matrix/Lyapunov matrix $[\mathbf{M}(t)]$ transforms an initial separation $\delta(0)$ to the separation $\delta(t)$ as $\delta(t) = \mathbf{M}(t) \delta(0)$. Then the evolution of deformation matrix is governed by Jacobian $\mathbf{J}(\mathbf{x}(t))$ as $\dot{\mathbf{M}}(t) = \mathbf{J}(\mathbf{x}(t))\mathbf{M}(t)$. Given the eigenvalues β_i of the matrix $\mathbf{M}^T(t)\mathbf{M}(t)$, the finite time Lyapunov exponents are defined as

$$\lambda_i(t) = \frac{\ln \beta_i(t)}{2t}. \quad (12)$$

To avoid the fluctuations in $\lambda_i(t)$, the infinite time limit is usually taken, which will lead us to the definition of the large-time Lyapunov exponents as

$$\lambda_i = \limsup_{t \rightarrow \infty} \lambda_i(t). \quad (13)$$

The system considered here [Eqs. (2)] has four phase-space dimensions and admits four large-time Lyapunov exponents, represented as Lyapunov spectrum $(\lambda_1, \lambda_2, \lambda_3, \lambda_4)$. The sign of the Lyapunov spectrum may be used to characterize the behavior of the system. A particle trajectory with a Lyapunov spectrum with signs $(+, 0, -, -)$ indicates chaotic, dynamics while $(0, -, -, -)$ indicates regular dynamics. The time evolution of the Lyapunov spectrum evaluated using the classic algorithm by Benettin *et al.* [39] for typical ballistic, trapped (in a Limit cycle), and chaotic trajectories for $St = 1.18$ particles is shown in Fig. 3(a). To account for numerical errors, Lyapunov exponents $\lambda_i < 5 \times 10^{-3}$ after $T = 10^4$ are set to zero. It is evident that both ballistic and trapped trajectories show regular dynamics, while the diffusive trajectory is chaotic. In Fig. 3(b) the Lyapunov spectrum corresponding to a particle which will be trapped at a SP at the large time limit is shown. For fixed point attractors, the Lyapunov exponents are the real part of the eigenvalues of linearized stability matrix [44]. Thus, here the spectrum asymptotically approaches sign $(+, -, -, -)$. For more details on the relation of the sign of the Lyapunov spectrum to the behavior of a dynamical system; see [45–47].

Since our system is dissipative, the sum of all four Lyapunov exponents for any trajectory is negative and equal to $-2/St$. Also, from numerical results, we can verify the symmetry (or conjugate pairing) of large-time Lyapunov exponents as $\lambda_1 + \lambda_4 = \lambda_2 + \lambda_3 = -1/St$, as seen in Fig. 3 (this symmetry is dynamically significant; see, e.g., [48–50]). Thus, only two of the four Lyapunov exponents are independent, say, λ_1 and λ_2 , and are sufficient to classify the trajectories. This can be seen as implemented in Fig. 4(a), which shows a scatterplot of the combinations of λ_1 and λ_2 for all trajectories. We see that trajectories naturally cluster into groups with similar dynamical behavior. In general, following the Lyapunov spectrum classification mentioned earlier, a cluster on the horizontal axis would have chaotic behavior, and the cluster on the vertical axis would have regular behavior. For the case of $St = 1.18$ particles shown in Fig. 4(a), the horizontal

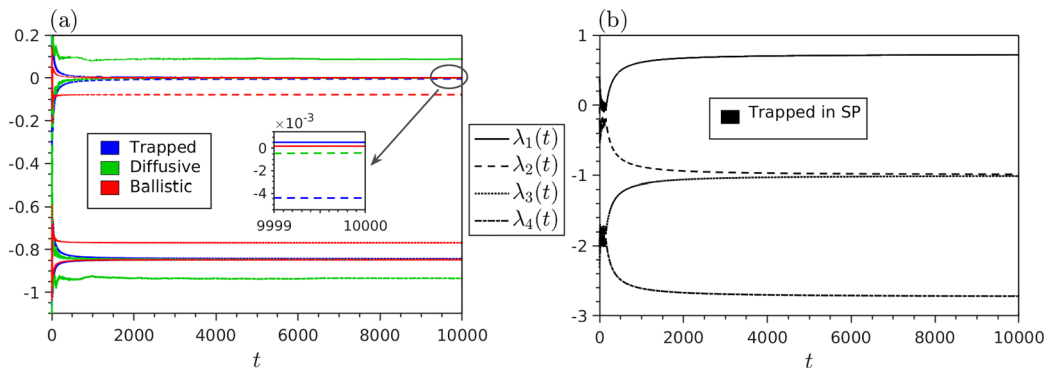


FIG. 3. The time evolution of Lyapunov exponents $\lambda_i(t)$ for (a) three $St = 1.18$ particles showing trapped (regular), diffusive (chaotic), and ballistic (regular) dispersion at the large time respectively starting at positions $(1.5, 0.5)$, $(0.55, 0.15)$, and $(0.5, 1.0)$ and (b) $St = 0.5$ particle starting at initial position $(1.5, 0.5)$ and getting trapped (in a SP) at the large time. The initial velocity of the particles in all the cases is fixed to be zero. Observe the symmetry of the Lyapunov spectrum in each case.

axis contains a single green cluster, showing chaotic particles. In the vertical axis, there are two clusters, i.e., two kinds of particles with regular dynamics. The red group shows particles with ballistic behavior, and the blue shows particles with trapped (in limit cycle) behavior. We use the same color code of trapped: blue, diffusive: green, and ballistic: red throughout this paper unless otherwise specified. Here we distinguished the ballistic and trapped particles, both of which show regular dynamics using the quantities α or v_m in addition to the Lyapunov exponents.

Similarly, Fig. 4(b) shows the histogram of the Lyapunov exponents λ_1 and $-\lambda_2$ for $St = 1.18$ particles. Again, the multimodality of the histogram suggests that the large time dynamics of all the particles are not identical, a hint of ergodicity breaking, which is contrary to what is observed by Wang *et al.* [11]. The apparent spread in the distribution of Lyapunov exponents for the ballistic or trapped (regular) regime [cf. the spread of α and v_m in Fig. 2(a) and 2(b)] is an artifact of the binning algorithm.

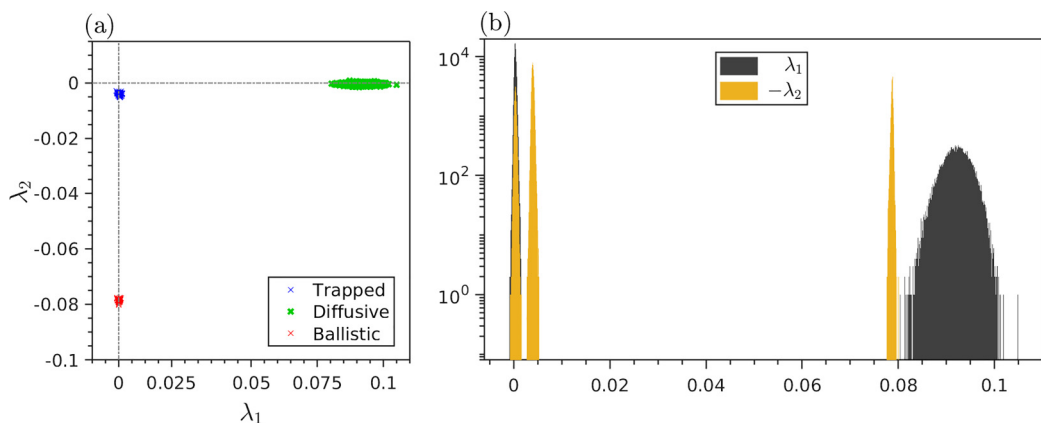


FIG. 4. (a) Distribution of large-time Lyapunov exponents of 316×316 trajectories with $St = 1.18$ (starting from basic vortex cell at uniformly distributed locations, with zero initial velocity) after $T = 10^4$ plotted in the λ_1 - λ_2 plane. (b) Histograms, generated with 1000 bins, of the Lyapunov exponents λ_1 and $-\lambda_2$ of 316×316 $St = 1.18$ particles, simulated up to 10^5 nondimensional time units.

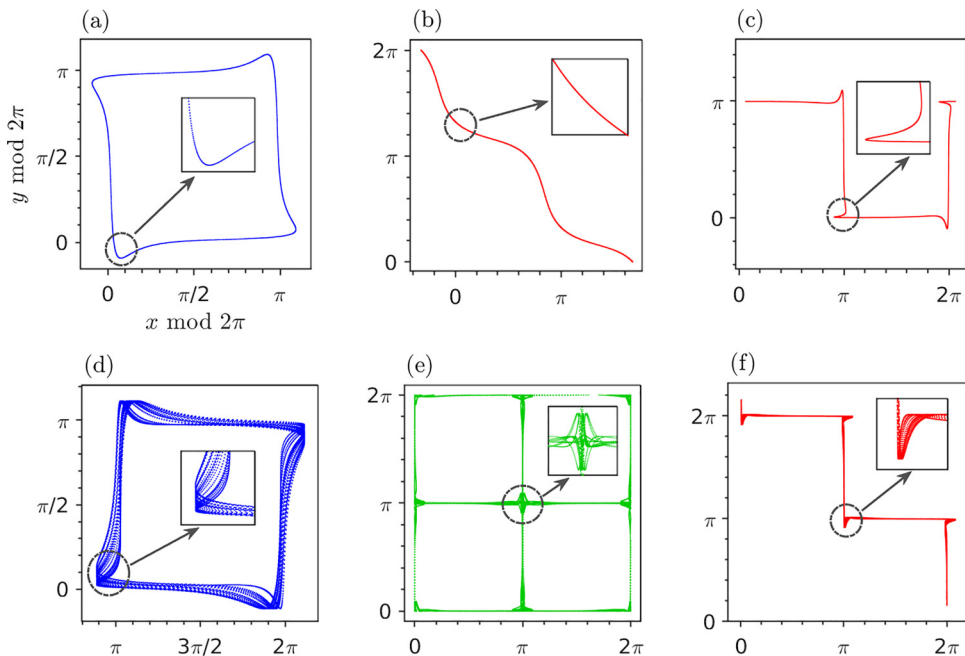


FIG. 5. Trajectories in the stationary state [i.e., $t \in (10^3, 10^4)$] showing typical dynamics, for particles initialized (a) at $(1.0, 0.42)$ with $St = 1.12$ (trapped-regular), (b) at $(2.48, 1.07)$ with $St = 1.83$ (smooth ballistic-regular, diagonal), (c) at $(1.5, 1.5)$ with $St = 1.133$ (ballistic-regular, horizontal, and square type), (d) at $(2.33, 0.81)$ with $St = 1.37$ (trapped-chaotic), (e) at $(0.11, 2.59)$ with $St = 1.12$ (diffusive-chaotic), and (f) at $(0.25, 0.5)$ with $St = 1.06$ (ballistic-chaotic). The insets show zoomed-in views near SP regions. A vertical ballistic trajectory similar to (c) also exists in rare parameter combinations, which is not shown here.

D. Trajectories in compactified ($\text{mod } 2\pi$) physical space

Visualizing the trajectories is a simple way of distinguishing regular and chaotic trajectories. In order to visualize both unbounded and bounded trajectories in a confined region, we plot the compactified coordinates $[x(\text{mod } 2\pi), y(\text{mod } 2\pi)]$ following [11]. The large-time [$t \in (10^3, 10^4)$] stationary dynamics for representative trajectories are shown in Fig. 5. Note that, in Fig. 5, the ranges of ordinate and abscissa are shifted manually to ensure the continuity of the curves.

The regular trajectories are of two types: Fig. 5(a) shows the projection of a regular, periodic simple closed curve, which is a limit cycle in the four-dimensional phase space; on the other hand, Figs. 5(b) and 5(c) show regular, ballistic, and thus unbounded trajectories appear as isolated open curves. Note that Fig. 5(b) is for a smooth ballistic trajectory with diagonal propagation, while Fig. 5(c) is for a square-type ballistic trajectory with horizontal propagation. Diagonally propagating trajectories are more common, and horizontally or vertically propagating trajectories are rare, as we observed from numerical simulations.

For a particle with chaotic-diffusive dynamics, the phase portrait will be space filling [see Fig. 5(e)], unlike simple curves. The space filling is mainly around the region of SPs. Though generally, the chaotic dynamics is exhibited by diffusively dispersing particles, some exceptions also exist. Trapped and ballistic trajectories can be chaotic as well; this is evident in Figs. 5(d) and 5(f), respectively. This space-filling nature of trajectories indicates the existence of a fractal or strange attractor.

E. Autocorrelation function

Yet another quantity that can be evaluated to distinguish between regular and chaotic dynamics qualitatively is the autocorrelation function. For an observable measured along the trajectory of a

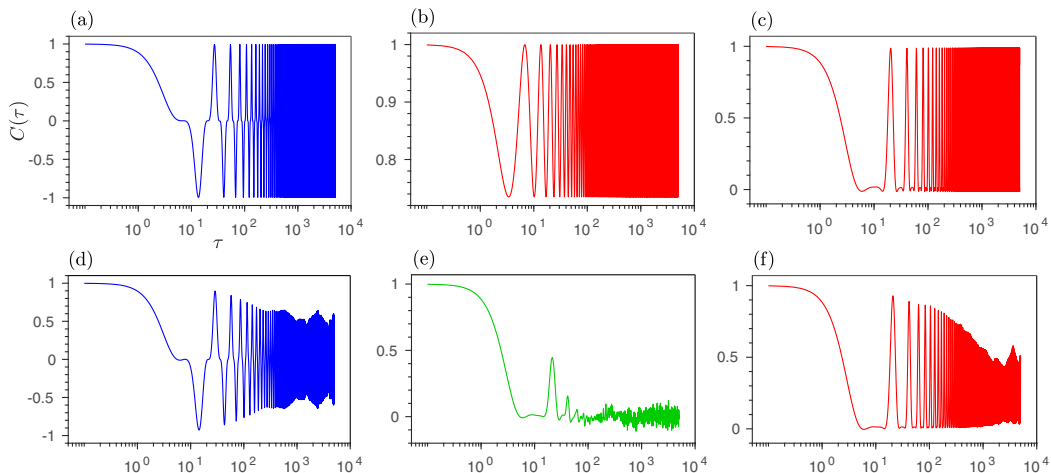


FIG. 6. The autocorrelation function $C(\tau)$ for representative trajectories of the different types mentioned in the text (cf. Fig. 5). The horizontal velocity $v_x(t)$ is used to calculate $C(\tau)$ [see Eq. (14)]. The same color scheme as Fig. 5 is used here.

particle $f(t)$, the autocorrelation function is defined (e.g., [17]) as

$$C(\tau) = \frac{\overline{f(t)f(t+\tau)}}{\overline{f(t)^2}}. \quad (14)$$

While $f(t)$ can be any observable like $x(t)$, $y(t)$, $v_x(t)$, $v_y(t)$, $z(t)$, $w(t)$, $v_z(t)$, and $v_w(t)$, bounded quantities are found to work best, especially for unbounded trajectories. The autocorrelation function, as defined, is normalized to lie between -1 and 1 . Thus, if $C(\tau)$ does not decay with time and has repeating peaks that reach up to unity, we may infer that the trajectory is regular; on the other hand, chaotic trajectories have decaying $C(\tau)$. A quantitative extension for distinguishing regular and chaotic dynamics would be the correlation dimension D_c , where the integrated squared autocorrelation function $C_{\text{int}}(t) = t^{-1} \int_0^t \|C(\tau)\|^2 d\tau$ for a state with purely singular continuous spectrum should decay as $\sim t^{-D_c}$ [17].

The autocorrelation function, evaluated using $v_x(t)$ as the observable, is plotted for representative trajectories in Fig. 6. For trapped or ballistic regular trajectories, $C(\tau)$ shows repeating peaks with magnitude unity [see Figs. 6(a)–6(c)]. On the other hand, for chaotic trajectories, $C(\tau)$ decays with time [see Figs. 6(d)–6(f)].

F. Frequency spectrum

The discrete Fourier transform (DFT) is closely related to the autocorrelation function, which provides an observable's frequency spectrum. The process is based on Fourier decomposing the time signal into various frequency components. Similar to the autocorrelation function, bounded quantities are preferred in the evaluation of the frequency spectrum as well. Figure 7 shows the frequency spectrum of representative large-time dynamics exhibited by inertial particles, showing that the frequency spectrum peaks at discrete values for regular trajectories. In contrast, it is more like a continuous band for chaotic (and thus aperiodic) trajectories. In Figs. 7(d) and 7(f), we see high-amplitude distinct peaks as well as low amplitudes between the peaks, corresponding to a definite mean shape of the trajectory with chaotic deviations from the mean.

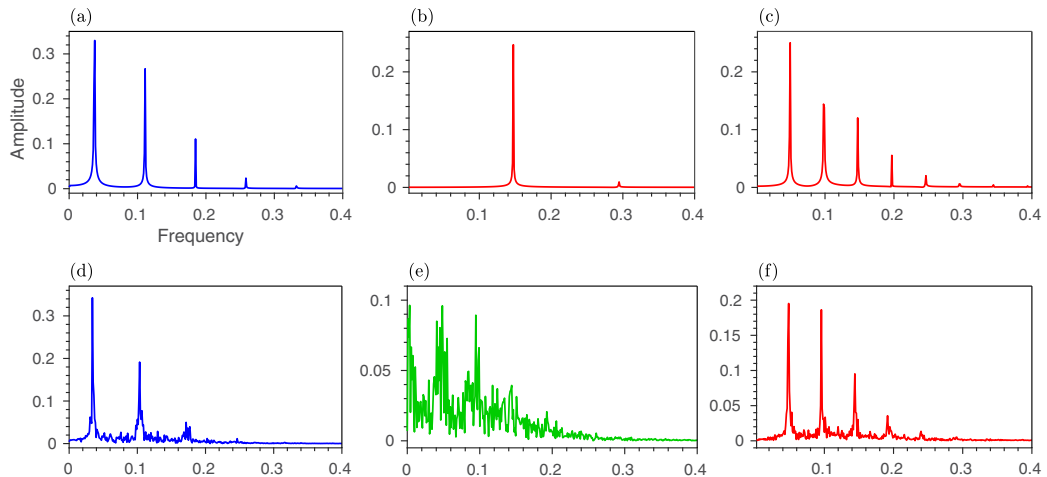


FIG. 7. Frequency spectrum for the representative trajectories in Figs. 5 or 6. The DFT is performed with a sampling frequency of 0.1. We note that square-type trajectories display a larger multiplicity of frequencies than smooth trajectories.

IV. RESULTS AND DISCUSSION

We have classified the particle trajectories as trapped, diffusive and ballistic based on their large-time dispersive characteristics. Also, based on their large-time dynamical behavior, we classified them as regular or chaotic. We observe that these classifications are sensitive to the initial positions $[x(0), y(0)]$ as well as inertia (St) of the particles. We found that the system is nonergodic, unlike in the case of turbulent flows. The nonergodicity of our system is reflected in the multimodal distribution of α , v_m and large-time Lyapunov exponents (λ_1 and λ_2), as can be seen in Figs. 2 and 4(b). We represent the dispersive and dynamical classifications in the colormaps in the upcoming subsection. We also quantify the fraction of particles exhibiting each dynamics as a function of Stokes number in Sec. IV B. The effect of the nonzero initial velocity of particles and periodicity of TG vortex flow is also analyzed subsequently.

A. Basin of large-time dynamics

One of our central findings is that bounded and unbounded trajectories may both occur for heavy particles of a given Stokes number and that their initial positions determine their fate. The domain of initial particle locations in the basic vortex cell consists of disjointed regions, each with distinct large-time dispersion or dynamics. Thus the behavior of inertial particles in the TG vortex flow is nonergodic.

An example is shown for $St = 1.18$ in Fig. 8(a), bottom, showing regions where trapped, diffusive, and ballistic trajectories originate in blue, green, and red, respectively. The trajectories were segregated by evaluating the SD, then α as mentioned in Sec. III A. The Fig. 8(a), bottom, plane is thus a colormap of α , where $\sigma^2(t) \sim t^\alpha$ in the limit of $t \rightarrow \infty$. Thus we classify the particle's initial conditions, which will result in a particular large-time dispersion. The collection of all those initial conditions is termed the “basin of that particular large-time dispersion.” For example, in Fig. 8(a), bottom, the red region corresponds to the basin of ballistic dispersion, the green region corresponds to diffusive dispersion, and the blue region corresponds to trapped dispersion. In Fig. 8(b) we plot the corresponding SD for typical (individual) trapped, diffusive, and ballistic trajectories. The scaling of SD with t^α is evident in the figure. The SD of trapped particles fluctuates about a mean saturated value, indicating being trapped in a periodic limit cycle, whereas the quadratic increase of SD for the ballistic trajectory is evident. The accurate identification of α is harder for individual

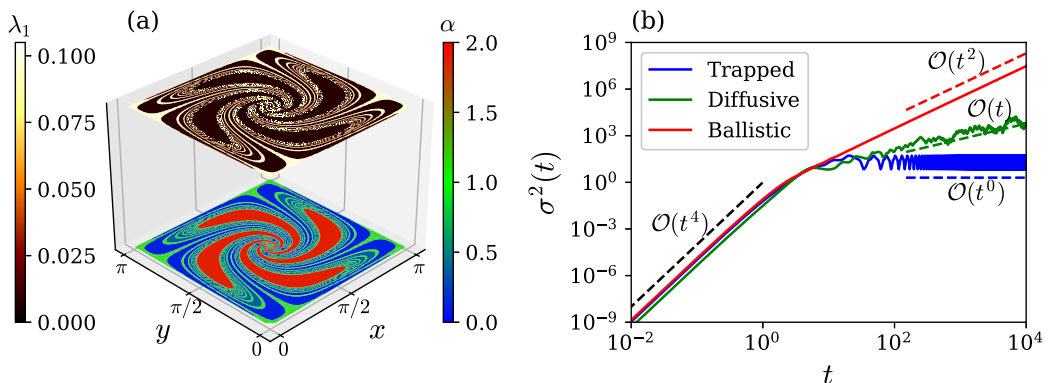


FIG. 8. (a) Colormaps, with 316×316 particles and $St = 1.18$, of (bottom) α such that $\sigma^2(t) \sim t^\alpha$ at large times, and (top) λ_1 , the largest of the “large-time Lyapunov exponents.” (b) $\sigma^2(t)$ (solid lines) for particles starting at $(1.5, 0.5)$, $(0.53, 0.15)$, and $(0.5, 1.0)$ and displaying typical ballistic, diffusive, and trapped large-time dispersive behavior, respectively; dashed lines show the corresponding scalings.

diffusive trajectories, e.g., to distinguish between normal ($\alpha = 1$) and anomalous ($\alpha \neq 1$) diffusion. So we first segregated ballistic and trapped trajectories using methods in Secs. III A and III B and collectively termed the remaining as “diffusive” (colored green). Then we used the colormap of α to obtain the pattern in Fig. 8(a), bottom. The pattern is four-petaled, which we suppose is the result of the square symmetry of the TG vortex flowfield. The pattern has been evaluated for the basic vortex cell. However, it will repeat symmetrically and periodically as we evaluate it for the other vortex cells, owing to the symmetry and periodicity of the TG vortex flowfield.

The same pattern emerges again if we use the colormap of large-time Lyapunov exponents, as seen in Fig. 8(a), top, which we refer to the “basin of large-time dynamics.” The brown region corresponds to regular dynamics, whereas the yellow region corresponds to chaotic dynamics. The correlation between positive λ_1 regions to diffusive regions and zero λ_1 regions to trapped or ballistic regions is clear from the figure. For example, at $St = 1.18$, ballistic or trapped particles show regular dynamics and correlate strongly with a periodic Lyapunov spectrum, while diffusive particles show chaotic dynamics and correlate strongly with a chaotic Lyapunov spectrum. This is true in general, except for certain St cases, the ballistic or trapped trajectories can also show chaotic behavior, as we have seen in some earlier cases [e.g., see Figs. 5(d) and 5(f)]. The exceptional cases will be more evident when we evaluate the fraction of particles involved in each kind of dynamics in the following subsection. Furthermore, the basin is fractal in nature. This is seen, e.g., by examining the Lyapunov dimension or Kaplan-Yorke dimension [51] D_{KY} , which shows qualitative features similar to the plots in Fig. 8. For $St = 1.18$ particles, we find $D_{KY} \approx 1$ for the nonchaotic region (brown) and $D_{KY} \approx 2.11$ for the chaotic region (yellow), consistent with one-dimensional attractors (simple curves) and space-filling curves, respectively.

We also note that for very early times ($t \ll 1$), $\sigma^2 \sim t^4$ [see Fig. 8(b)]; i.e., the dynamics is “super-ballistic” for all initial particle locations. This can be explained as follows. For particles starting with zero initial velocity, the system of Eqs. (2) becomes $St\ddot{x}(0) = \sin x(0) \cos y(0)$ and $St\ddot{y}(0) = -\sin y(0) \cos x(0)$ at the initial instant: i.e., initially the particles experience acceleration due to the flow. For $t \ll 1$, the approximate solution can be then obtained as $x(t) \approx x(0) + \sin x(0) \cos y(0) t^2 / (2 St)$ and $y(t) \approx y(0) - \sin y(0) \cos x(0) t^2 / (2 St)$. These solutions yield $\sigma^2(t) \approx [\sin^2 x(0) \cos^2 y(0) + \sin^2 y(0) \cos^2 x(0)] t^4 / (4 St^2)$; i.e., $\sigma \sim t^4$ when $t \ll 1$.

B. Fraction of particles exhibiting each kind of behavior

Another central finding is the sensitivity of dynamics to inertia or Stokes number. The total fraction of particles that exhibit each kind of behavior versus the Stokes number in the range

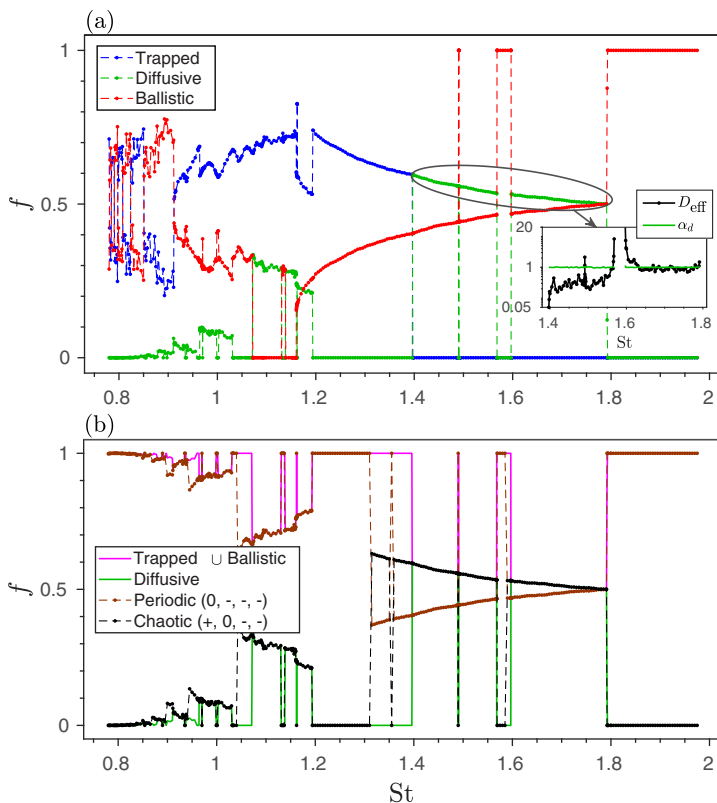


FIG. 9. (a) Fraction, f , of trapped, diffusive, and ballistic particles. The inset shows effective diffusivity D_{eff} (black) and the average α (green) of diffusive particles. $\alpha_d \approx 1$ indicates normal diffusion. (b) The fraction (f) of particles with regular and chaotic Lyapunov spectrum are plotted for various Stokes numbers. The fraction of (trapped \cup ballistic) particles and diffusive particles are shown in the background using light colors. The one-to-one mapping between the two kinds of classification is evident (excluding certain windows of Stokes number).

$0.78 \leq St \leq 1.975$ is plotted in Fig. 9. The fraction of particles exhibiting trapped, diffusive, or ballistic dispersion is shown in Fig. 9(a), corresponding to the respective fraction of each category's area in the basin of large-time dispersion. In Fig. 9(b), on the contrary, we represent the fraction of particles that exhibit regular or chaotic dynamics, which is identified from the corresponding Lyapunov exponents. Also, in light colors, the fraction of particles exhibiting trapped or ballistic and diffusive dispersion is superimposed in Fig. 9(b) for comparison. One can observe that the fraction of trapped or ballistic particles matches well with the fraction of particles with regular dynamics; similarly, the fraction of diffusive particles matches well with that of the chaotic particles. This close correspondence between these two different kinds of plots suggests that almost all the diffusive particles exhibit diffusive dynamics; similarly, almost all ballistic or trapped particles exhibit regular periodic dynamics. However, this observation is not valid for all values of Stokes numbers, as can be inferred from a close inspection of Fig. 9(b). There exist more than one small windows of St where this correspondence fails. A typical example has been shown earlier in Figs. 5(d) and 5(f), where particles exhibiting trapped or ballistic dispersion can also show chaotic dynamics. Nevertheless, this behavior is rare and happens only for a few small windows of Stokes numbers, which appear as the mismatch windows in Fig. 9(b). The main conclusion of the existence of each kind of dispersion or dynamics with Stokes number is summarized in Table I.

TABLE I. Different large-time dispersion characteristics and dynamical nature for various St intervals obtained from numerical simulations. The \checkmark indicates existence, and \times indicates the absence of a particular characteristic. The diversity in the dynamical behavior for a particular value of St is the result of the IC dependence of the dynamical system.

| Range of St | Trapped | Diffusive | Ballistic | Regular | Chaotic |
|-------------------------------------------------------------|--------------|--------------|--------------|--------------|--------------|
| $(1.791, \infty) \cup (1.5688, 1.59) \cup (1.4898, 1.4902)$ | \times | \times | \checkmark | \checkmark | \times |
| $(1.597, 1.791) \cup (1.49116, 1.568) \cup (1.396, 1.4898)$ | \times | \checkmark | \checkmark | \checkmark | \checkmark |
| $(1.59, 1.597) \cup (1.568, 1.5688) \cup (1.4902, 1.49116)$ | \times | \times | \checkmark | \checkmark | \checkmark |
| $(1.36, 1.396) \cup (1.31, 1.35) \cup (1.137, 1.139)$ | \checkmark | \times | \checkmark | \checkmark | \checkmark |
| $\cup(1.04, 1.072) \cup (1.001, 1.003) \cup (0.96, 0.9642)$ | | | | | |
| $(1.35, 1.36) \cup (1.193, 1.31) \cup (1.1618, 1.1625)$ | \checkmark | \times | \checkmark | \checkmark | \times |
| $\cup(1.13, 1.137) \cup (1.03, 1.04) \cup (0.998, 1.001)$ | | | | | |
| $\cup(0.9699, 0.9701)$ | | | | | |
| $(1.1625, 1.193) \cup (1.1602, 1.1618) \cup (1.003, 1.03)$ | \checkmark | \checkmark | \checkmark | \checkmark | \checkmark |
| $\cup(0.9701, 0.998) \cup (0.9642, 0.9699)$ | | | | | |
| $(1.139, 1.1602) \cup (1.072, 1.13)$ | \checkmark | \checkmark | \times | \checkmark | \checkmark |
| $(0, 0.77)$ | \checkmark | \times | \times | \checkmark | \times |

The general resolution in the St axis in Fig. 9 is 5×10^{-3} . However, certain ranges in the St axis are resolved further up to 4×10^{-5} to capture smaller windows of Stokes number displaying abrupt variations. The bifurcation diagram in Fig. 13 in Appendix B shows evidence of such smaller windows, which we have missed in Fig. 9.

All three diffusive behaviors (trapped, diffusive, and ballistic) coexist only in some intervals, as can be seen from Table I. $St = 1.18$, chosen here for most figures, lies within such an interval. Incidentally, the ballistic dispersion is absent in the interval $St \in (1.072, 1.13) \cup (1.139, 1.1602)$. Assuming that one gradually increases the Stokes number of a heavy particle started with appropriate ICs in the TG vortex, the particle is expected to show ballistic dispersion when $St \sim 1$. But, when the $St \in (1.072, 1.13) \cup (1.139, 1.1602)$, the particle will switch to nonballistic transport. As the St again increases, the particle will revert to ballistic transport after these windows. This exact behavior can be seen in action in the case of transport of condensing water droplets in a TG vortex [33] (Fig. 11). The mean square displacement (MSD) of water droplets approach from super-diffusive to ballistic dispersion through a steplike approach as their instantaneous Stokes number $St(t) \gtrsim 1$. Also, as the particles' dominant transport becomes ballistic, the droplets' spatial distribution changes from isotropic to diagonally dominated anisotropic distribution, consistent with our results.

The roughness as a function of Stokes number is evident in Fig. 9. The noisiness of the curves, especially for $St \lesssim 1$, is intrinsic to the dynamics and not a numerical feature. We claim that this roughness is due to an intrinsic fractal nature and cannot be eliminated by any means. A supporting argument is as follows: For $St \in (1.396, 1.791)$, we find that the SD averaged over the set of diffusive particle trajectories, $\langle \sigma_D^2(t) \rangle$, scales linearly with time, indicating normal diffusion ($\alpha \approx 1$).

Thus, we may evaluate their effective diffusivity as $D_{\text{eff}} = \lim_{t \rightarrow \infty} \frac{1}{4} \frac{d\langle \sigma_D^2(t) \rangle}{dt}$, which is plotted as an inset in Fig. 9(a). The variation of D_{eff} also shows a rough trend with St. This is identical to the rough variation of the diffusion coefficient with energy parameter in [21]. Notice that, in the windows of Stokes number of purely ballistic motion ($1.597 \gtrsim St \gtrsim 1.568$ and $1.49116 \gtrsim St \gtrsim 1.4902$), the effective diffusivity diverges, indicating the absence of normal diffusion. In those intervals, instead, super- (ballistic) diffusion happens.

Furthermore, all particles with $St \lesssim 0.77$ are attracted to fixed points (SPs) and thus have a $(+, -, -, -)$ Lyapunov spectrum, in the limit $t \rightarrow \infty$. It is well known that for trajectories attracted to fixed points, the large-time Lyapunov exponents are the real part of the eigenvalues of the linearized stability matrix about those fixed points [44]. Thus, $\lambda_1 > 0$ here indicates only the saddle

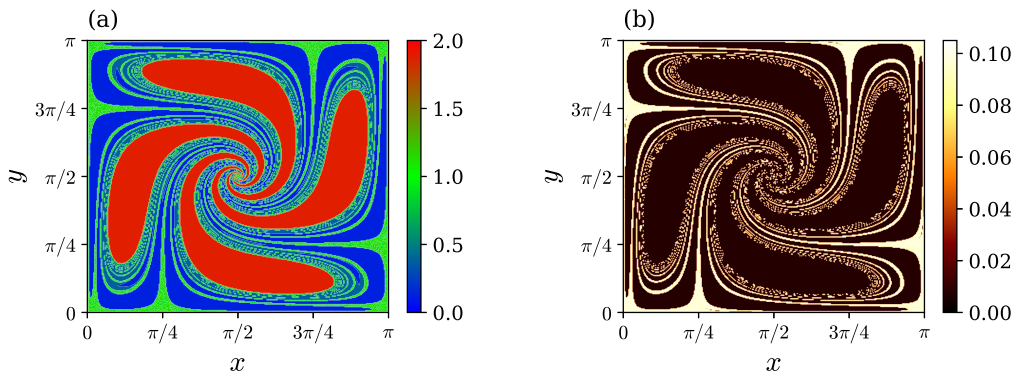


FIG. 10. Colormaps of (a) α , similar to Fig. 8(a), bottom, and (b) the large-time Lyapunov exponent λ_1 similar to Fig. 8(a), top, with the same parameters as in those figures except with the initial particle velocity set equal to the local fluid velocity.

nature of the fixed point and not any chaotic nature. Otherwise, at least one of the Lyapunov exponents must vanish in the Lyapunov spectrum [52], which does not happen here as the spectrum is $(+, -, -, -)$.

C. Effect of nonzero initial velocity

In all the results reported in this paper until now, the simulations are initialized with particles uniformly distributed in the basic vortex cell with zero initial velocity, i.e., $v_x(0) = v_y(0) = 0$. Here we examine the effect of a different choice of initial velocity, setting the initial particle velocity equal to the local fluid velocity [i.e., $v_x(0) = \sin x(0) \cos y(0)$ and $v_y(0) = -\cos x(0) \sin y(0)$], no-slip. We solve Eqs. (2), with initial positions being the uniformly sampled locations in the basic vortex cell and the initial velocities being the local fluid velocity. In contrast to the zero initial velocity case, here, initially, particles experience no initial acceleration due to no-slip. Thus, the solutions at the initial stages are linear in time as $x(t) \approx x(0) + \sin x(0) \cos y(0)t$ and $y(t) \approx y(0) - \sin y(0) \cos x(0)t$. The SD can then shown to vary as $\sigma^2(t) \approx [\sin^2 x(0) \cos^2 y(0) + \sin^2 y(0) \cos^2 x(0)]t^2$ [i.e., $\sigma^2(t) \sim t^2$] for $t \ll 1$. In other words, particles starting with no-slip behave ballistically at the initial time due to their nonzero initial velocity in contrast to those starting with zero velocity (which behave super ballistically due to their initial acceleration, as explained in Sec. IV A). However, the system behaves qualitatively the same in both cases at large times if one plots the SD (not shown here).

The basins of large-time dispersion and large-time dynamics are shown in Fig. 10. The results with the two choices of initial velocity are qualitatively similar can be seen by comparing Fig. 10 with Fig. 8. We find that particles with nonzero initial velocity also show diverse large-time dispersion (trapped, diffusive, or ballistic) and diverse large-time dynamics (regular or chaotic) when $St \sim 1$, depending on their initial positions. Thus, irrespective of the initial velocity condition, we find nonergodic behavior.

Similarly, the correspondence between trapped or ballistic dispersion with periodic dynamics (and diffusive dispersion with chaotic dynamics) continues to exist for most Stokes numbers. This may be seen by comparing the colourmap of the dispersion exponent α in Fig. 10(a) with the colourmap of the Lyapunov exponent λ_1 in Fig. 10(b).

While the zero-velocity and zero-slip ICs lead to similar qualitative behavior at large time, we see a clear quantitative difference. The fraction of ballistic particles in the case of zero initial velocity is 23.56%; whereas a higher fraction, 31.88%, of particles starting with no-slip ICs have ballistic long-term behavior with a corresponding reduction in the fraction displaying diffusive or trapped behavior. We suspect that the initial ballistic dynamics of *all* particles for zero-slip ICs (in contrast

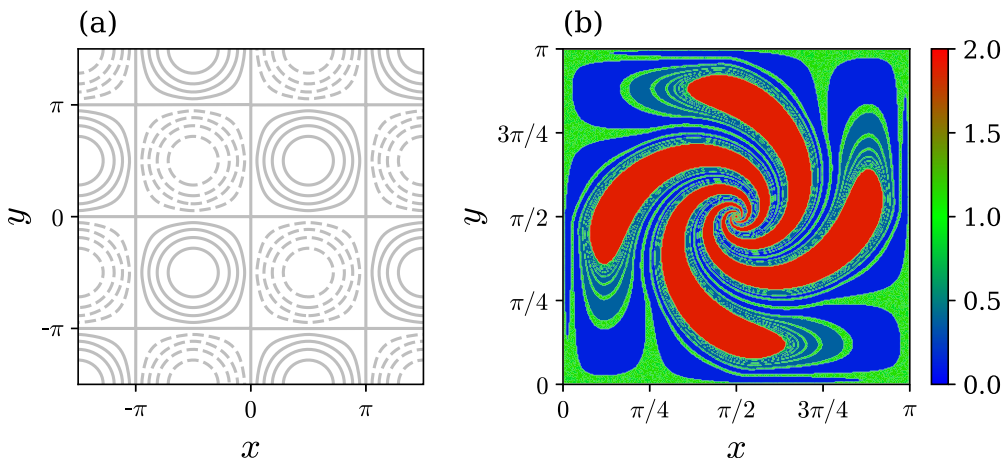


FIG. 11. (a) Streamlines of the triangular flow field. Observe the qualitative similarity of the flowfield with the TG vortex flow field shown in the background of Fig. 1(b). (b) Color map of α , indicative of the large-time dynamics, of 316×316 inertial particles with $St = 1.15$ initialized uniformly in the basic vortex cell $(0, \pi) \times (0, \pi)$ of triangular flow; trapped (blue), diffusive (green), and ballistic (red) trajectories are possible at this Stokes number.

to the initial hyperballistic dynamics for zero velocity ICs) have contributed in this regard. However, to systematically show this, one must study the dependence of all possible initial velocities and all possible initial positions in a four-dimensional IC-space. Nevertheless, the two cases presented here, i.e., (1) zero initial velocity and (2) initial velocity as the same as local fluid velocity (no-slip), are most representative of particles in a turbulent flow (see, e.g., [53]).

D. Effect of periodicity of the background flow

The dynamical richness we observe in the simple system Eqs. (2) or (3) has to do with the perfect symmetry and periodicity of the TG vortex flow. However, here we argue that a different choice of the flowfield, which is topologically identical, can also show the same dynamical richness as long as the symmetry and periodicity are preserved. In analogy to the conjugacy of the logistic map and the tent map [41], we can replace the sinusoids in Eqs. (3) with triangular waves, i.e., $\sin z$ to $T(z)$ and $\sin w$ to $T(w)$, where the triangular wave T is defined as

$$T(\xi) = \begin{cases} \eta & \text{if } \eta \in [-\pi/2, \pi/2] \\ \pi - \eta & \text{if } \eta \in [\pi/2, 3\pi/2] \end{cases} \quad (15)$$

with $\eta = \text{mod}(\xi + \pi/2, 2\pi) - \pi/2$. The resulting flow is topologically similar to the TG vortex flow [see the streamlines of the flowfield in Fig. 11(a)]. Thus Eqs. (3) become

$$St \ddot{z} + \dot{z} = T(w), \quad (16a)$$

$$St \ddot{w} + \dot{w} = T(z), \quad (16b)$$

which describe the motion of a heavy inertial particle in a flowfield given by fluid velocities $u_x = [T(x - y) + T(x + y)]/2$ and $u_y = [T(x - y) - T(x + y)]/2$. We may refer to this flow as simply the “triangular flow” to distinguish it from TG vortex flow. The system can be solved analytically (see Appendix C), owing to the piecewise linearity and periodicity of the triangular wave. Using the analytical results, one can verify that the dynamical richness we observed in the TG vortex flowfield can also be observed in this new system as well. This correspondence is similar to the conjugacy between the (quadratic) logistic map and the (piecewise-linear) tent map [41]. The analytically tractable solution increases the believability of the results.

The correspondence between the TG vortex flow and the triangular flow is apparent in Fig. 11(b). The colormap of α in the figure is analogous to Fig. 8(a), bottom, and shows the existence of three kinds of asymptotic dispersive behavior—trapped, diffusive, or ballistic—depending upon the initial position of particles. The Stokes number chosen here, $St = 1.15$, is, however, different from but close to the Stokes number $St = 1.18$ in Fig. 8(b). Here we chose $St = 1.15$ because all three dispersive characteristics do not exist for $St = 1.18$ in triangular flow. From the similarity between Figs. 11(b) and 8(a), we conclude that the richness of the dynamics is reproduced by this synthetic flowfield.

V. CONCLUSION

We have shown that heavy inertial particles ($R = 0$) show a rich tapestry of dynamics even in a very simple two-dimensional cellular flow. The governing dynamical system resembles a billiard system—a viscous soft Lorentz gas, further confirmed by the diverse transport behaviors. The large-time dispersion of a particle is shown to be dependent nonmonotonically, and often extremely sensitively, on its inertia (Stokes number) and initial location. The dramatic changes in dispersion with minor changes in St are particularly counterintuitive. When $St \sim 1$, the initial positions in the flowfield corresponding to various large-time dispersion—trapped, diffusive, and ballistic—form disjoint groups. The trajectory of a particle starting from one such group can exhibit only one kind of large-time dynamics, indicating ergodicity breaking. For a range of Stokes numbers, for particles undergoing normal diffusion, the effective diffusivity depends irregularly on St , indicating the underlying fractal nature of the dynamics. The “fraction of particles” showing each kind of dispersion shows abrupt transitions as St varies.

We expect our findings in a TG vortex flow to be generally applicable in broad classes of flows containing periodic arrays of vortices and stagnation points. In turbulence too, while the background flow is highly unsteady, we expect signatures of ergodicity and irregular dependence on Stokes number, since local stagnation points and streamlines (separatrices) can last far longer than particle timescales. Thus, particles may have bounded and unbounded trajectories with positive Lyapunov exponents, affecting their interaction (collisions and coalescence).

ACKNOWLEDGMENTS

S.R. was supported at Nordita under the Swedish Research Council Grant No. 638-2013-9243. Nordita is partially supported by Nordforsk. S.R. is supported at IIT Bombay through seed Grant No. RD/0522-IRCCSH0-020. A.V.S.N. thanks the Prime Minister’s Research Fellows (PMRF) scheme, Ministry of Education, Government of India. R.G. acknowledges the support of the Department of Atomic Energy, Government of India, under Project No. RTI4001. A.R. and A.V.S.N. acknowledge the support of the Complex Systems and Dynamics Group at IIT Madras.

APPENDIX A: ACCURACY OF THE NUMERICAL SIMULATIONS

As mentioned in Sec. II, Eqs. (2) are integrated using a fourth-order Runge-Kutta method. The maximum time step for integration is 10^{-2} , and the equations are integrated for 10^4 or 10^5 nondimensional time units to obtain information about the large-time particle dynamics. Since we are dealing with Stokes numbers of $O(1)$, this time step is much smaller than the particle response timescale. However, since the dynamics involve not only regular but also chaotic nature, a further check on the accuracy of the numerical integration is required. We evaluate the constant of motion \mathcal{Q} for all the trajectories shown in Fig. 1. The integral term in the definition of \mathcal{Q} (see Sec. II) is evaluated using the trapezoidal rule, and the results are plotted in Fig. 12. We observe that the numerical solutions are accurate to better than 0.1% in the worst case, and the errors do not grow with time even after $t = 10^5$.

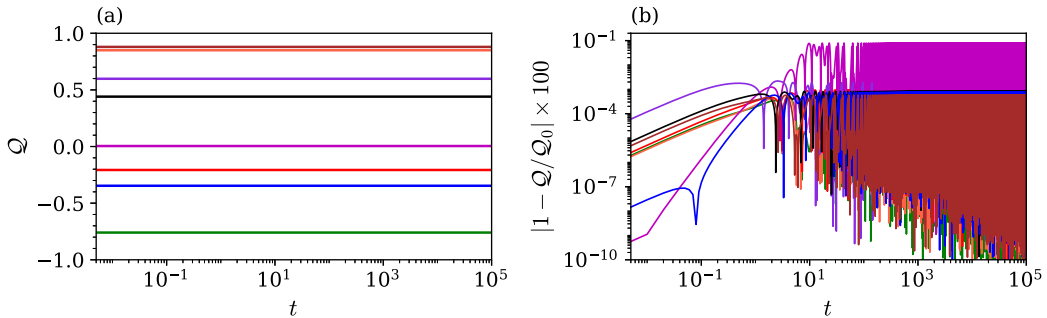


FIG. 12. (a) Evolution of constant of dynamics Q with time for the cases in Fig. 1 with the same color codes. (b) The percentage relative error in the numerically evaluated value of Q with the theoretically expected value Q_0 is plotted with time and shown to be negligible and bounded for all the cases until $t = 10^5$.

APPENDIX B: BIFURCATION DIAGRAM

A “bifurcation diagram” is a plot of some attribute of the system as a parameter, called the bifurcation parameter, is varied. In Fig. 13 we plot the local maxima of the bounded observable $v_x(t)$ vs the Stokes number. The trajectories are initialized from position $(2.33, 0.81)$ with zero initial velocity. As the Stokes number is varied, the local maxima of the $v_x(t)$ are identified and placed in a scatter plot to obtain Fig. 13.

We see that for $St \gtrsim 1.792$, the bifurcation plot is either a single-valued or bivalued curve showing that the dynamics is regular. However, when $St \lesssim 1.792$, the bifurcation plot has three dense bands, showing the chaotic nature of the dynamics. Similar abrupt variations in the dynamics exist in many intervals of Stokes numbers, as shown in the insets of Fig. 13. We have also used a resolution in St of $1.25 \times 10^{-4} < 5 \times 10^{-3}$ here, allowing sharper regular-chaotic transitions than in Fig. 9 to be captured. It can be seen that many of the small windows of the Stokes number we missed in Fig. 9 are captured in Fig. 13. This is due to the finer sampling of the Stokes axis, which is effortless here since we are dealing with only one initial particle position.

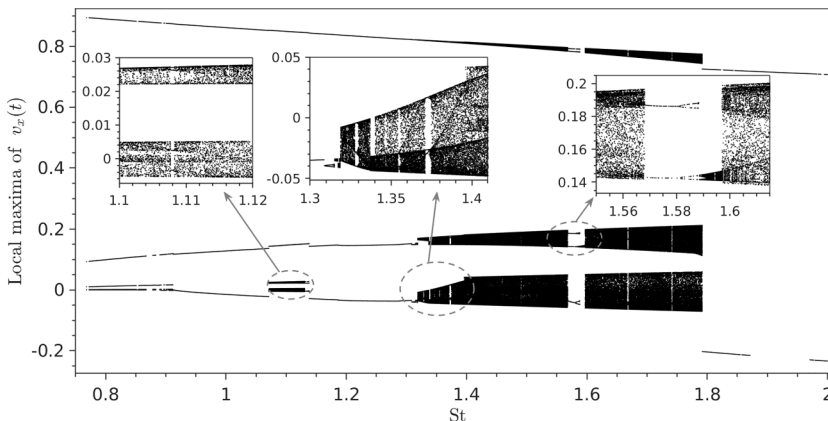


FIG. 13. Bifurcation diagram plotted using local maxima of $v_x(t)$ vs St for a particle starting at the initial location $(2.33, 0.81)$ with zero initial velocity. The values in the St axis ranges from 0.75 to 2. The insets zoom in on certain regions where the system transition from regular to chaotic dynamics as St is changed.

APPENDIX C: TRIANGULAR FLOW: ANALYTICAL SOLUTION

Since the triangular wave T is piecewise linear, Eqs. (16) can be solved analytically in subdomains of the flowfield, as shown below. We can then combine these solutions, using the fact that the flowfield is periodic, to obtain the exact trajectory tracking of a particle.

1. Case 1: When $z \in [-\pi/2, \pi/2)$ and $w \in [-\pi/2, \pi/2)$

In this interval, the governing equations Eqs. (16) can be simplified to

$$\text{St} \ddot{z} + \dot{z} = w, \quad (\text{C1a})$$

$$\text{St} \ddot{w} + \dot{w} = z. \quad (\text{C1b})$$

The trajectory of a particle entering this region at time $t = 0$ with initial conditions z_0, w_0, v_{z0}, v_{w0} can write analytically as

$$z(t) = A^+ e^{\alpha^+ t} - A^- e^{\alpha^- t} + e^{-t/2\text{St}} (y_0 \cos \beta t + D_1 \sin \beta t), \quad (\text{C2a})$$

$$w(t) = A^+ e^{\alpha^+ t} - A^- e^{\alpha^- t} - e^{-t/2\text{St}} (y_0 \cos \beta t + D_1 \sin \beta t), \quad (\text{C2b})$$

where $\text{St} > 1/4$ and

$$A^\pm = \frac{2 \text{St} v_{x0} + (1 \pm \sqrt{1 + 4 \text{St}}) x_0}{2 \sqrt{1 + 4 \text{St}}}, \quad (\text{C3a})$$

$$D_1 = \frac{2 \text{St} v_{y0} + y_0}{\sqrt{4 \text{St} - 1}}, \quad (\text{C3b})$$

$$\alpha^\pm = \frac{-1 \pm \sqrt{1 + 4 \text{St}}}{2 \text{St}}, \quad (\text{C3c})$$

$$\beta = \frac{\sqrt{4 \text{St} - 1}}{2 \text{St}}. \quad (\text{C3d})$$

Similarly, assuming the same notation for the initial conditions, as the particle enters other subdomains of the flowfield, the solutions in those domains are written as follows.

2. Case 2: When $z \in [\pi/2, 3\pi/2)$ and $w \in [-\pi/2, \pi/2)$

$$\text{St} \ddot{z} + \dot{z} = w, \quad (\text{C4a})$$

$$\text{St} \ddot{w} + \dot{w} = \pi - z, \quad (\text{C4b})$$

$$z(t) = \pi + e^{-t/2\text{St}} \{ \cosh(p^+ t) [K_1^+ \sin(p^- t) - (\pi - z_0) \cos(p^- t)] \\ + \sinh(p^+ t) [K_1^- \cos(p^- t) + w_0 \sin(p^- t)] \}, \quad (\text{C5a})$$

$$w(t) = e^{-t/2\text{St}} \{ \sinh(p^+ t) [K_1^+ \cos(p^- t) + (\pi - z_0) \sin(p^- t)] \\ + \cosh(p^+ t) [-K_1^- \sin(p^- t) + w_0 \cos(p^- t)] \}, \quad (\text{C5b})$$

where

$$p^\pm = \frac{\sqrt{2 \text{St} q \pm 1}}{2 \sqrt{2} \text{St}}, \quad (\text{C6a})$$

$$q = \frac{\sqrt{1 + 16 \text{St}^2}}{2 \text{St}}, \quad (\text{C6b})$$

$$K_1^\pm = \frac{-\pi p^\mp + p^+ C^\mp \pm p^- C^\pm}{q}, \quad (\text{C6c})$$

$$C^\pm = 2 \text{St} (v_{x0} \pm v_{y0}) + (x_0 \pm y_0). \quad (\text{C6d})$$

3. Case 3: When $z \in [\pi/2, 3\pi/2)$ and $w \in [\pi/2, 3\pi/2)$

$$\text{St} \ddot{z} + \dot{z} = \pi - w, \quad (\text{C7a})$$

$$\text{St} \ddot{w} + \dot{w} = \pi - z, \quad (\text{C7b})$$

$$z(t) = \pi + B^+ e^{\alpha^+ t} - B^- e^{\alpha^- t} - e^{-t/2\text{St}}[(\pi - x_0) \cos \beta t - D_2 \sin \beta t], \quad (\text{C8a})$$

$$w(t) = \pi - B^+ e^{\alpha^+ t} + B^- e^{\alpha^- t} - e^{-t/2\text{St}}[(\pi - x_0) \cos \beta t - D_2 \sin \beta t], \quad (\text{C8b})$$

where

$$B^\pm = \frac{2 \text{St} v_{y0} + (1 \pm \sqrt{1 + 4 \text{St}}) y_0}{2 \sqrt{1 + 4 \text{St}}}, \quad (\text{C9a})$$

$$D_2 = \frac{2 \text{St} v_{x0} + x_0 - \pi}{\sqrt{4 \text{St} - 1}}. \quad (\text{C9b})$$

4. Case 4: When $z \in [-\pi/2, \pi/2)$ and $w \in [\pi/2, 3\pi/2)$

$$\text{St} \ddot{z} + \dot{z} = \pi - w, \quad (\text{C10a})$$

$$\text{St} \ddot{w} + \dot{w} = z, \quad (\text{C10b})$$

$$z(t) = e^{-t/2\text{St}} \{ \cosh(p^+ t) [-K_2^+ \sin(p^- t) + z_0 \cos(p^- t)] \\ + \sinh(p^+ t) [K_2^- \cos(p^- t) + (\pi - w_0) \sin(p^- t)] \}, \quad (\text{C11a})$$

$$w(t) = \pi + e^{-t/2\text{St}} \{ \sinh(p^+ t) [K_2^+ \cos(p^- t) + z_0 \sin(p^- t)] \\ + \cosh(p^+ t) [K_2^- \sin(p^- t) - (\pi - w_0) \cos(p^- t)] \}, \quad (\text{C11b})$$

where

$$K_2^\pm = \frac{-\pi p^\pm + p^+ C^\mp \mp p^- C^\pm}{q}. \quad (\text{C12})$$

-
- [1] M. R. Maxey and J. J. Riley, Equation of motion for a small rigid sphere in a nonuniform flow, *Phys. Fluids* **26**, 883 (1983).
- [2] L. G. Leal, Studies of flow-induced conformation changes in dilute polymer solutions, in *Polymer-Flow Interactions 10-12 July 1985 La Jolla, CA, USA*, AIP Conf. Prof. 137 (AIP, Melville, NY, 1986), pp. 5–32.
- [3] B. Bentley and L. Leal, A computer-controlled four-roll mill for investigations of particle and drop dynamics in two-dimensional linear shear flows, *J. Fluid Mech.* **167**, 219 (1986).
- [4] P. T. Corona, N. Ruocco, K. M. Weigandt, L. G. Leal, and M. E. Helgeson, Probing flow-induced nanostructure of complex fluids in arbitrary 2D flows using a fluidic four-roll mill (FFoRM), *Sci. Rep.* **8**, 15559 (2018).
- [5] N. Burshtein, K. Zografos, A. Q. Shen, R. J. Poole, and S. J. Haward, Inertioelastic flow instability at a stagnation point, *Phys. Rev. X* **7**, 041039 (2017).
- [6] H. Stommel, Trajectories of small bodies sinking slowly through convection cells, *J. Mar. Res.* **8**, 24 (1949).
- [7] L. Bergougnoux, G. Bouchet, D. Lopez, and E. Guazzelli, The motion of solid spherical particles falling in a cellular flow field at low Stokes number, *Phys. Fluids* **26**, 093302 (2014).
- [8] D. Lopez and E. Guazzelli, Inertial effects on fibers settling in a vortical flow, *Phys. Rev. Fluids* **2**, 024306 (2017).

- [9] T. H. Solomon and J. P. Gollub, Chaotic particle transport in time-dependent Rayleigh-Bénard convection, *Phys. Rev. A* **38**, 6280 (1988).
- [10] K. M. S. Bajaj, J. Liu, B. Naberhuis, and G. Ahlers, Square patterns in Rayleigh-Bénard convection with rotation about a vertical axis, *Phys. Rev. Lett.* **81**, 806 (1998).
- [11] L. Wang, M. Maxey, T. Burton, and D. Stock, Chaotic dynamics of particle dispersion in fluids, *Phys. Fluids* **4**, 1789 (1992).
- [12] H. E. Nusse, E. Ott, and J. A. Yorke, Saddle-node bifurcations on fractal basin boundaries, *Phys. Rev. Lett.* **75**, 2482 (1995).
- [13] C. A. Kitio Kwiimy, C. Nataraj, and M. Belhaq, Chaos in a magnetic pendulum subjected to tilted excitation and parametric damping, *Math. Probl. Eng.* **2012**, 546364 (2012).
- [14] R. Klages, *Microscopic Chaos, Fractals and Transport in Nonequilibrium Statistical Mechanics*, Advanced Series in Nonlinear Dynamics, Vol. 24 (World Scientific, 2007).
- [15] B. V. Chirikov, Research concerning the theory of non-linear resonance and stochasticity, Tech. Rep. CM-P00100691 (CERN Libraries, Geneva, 1971).
- [16] B. P. Wood, A. J. Lichtenberg, and M. A. Lieberman, Arnold diffusion in weakly coupled standard maps, *Phys. Rev. A* **42**, 5885 (1990).
- [17] M. A. Zaks, A. S. Pikovsky, and J. Kurths, Steady viscous flow with fractal power spectrum, *Phys. Rev. Lett.* **77**, 4338 (1996).
- [18] M. A. Zaks and A. Nepomnyashchy, Subdiffusive and superdiffusive transport in plane steady viscous flows, *Proc. Natl. Acad. Sci. USA* **116**, 18245 (2019).
- [19] B. S. Maryshev and M. A. Zaks, Modelling of transportation process in plane flows with stagnation points, *Transp. Porous Media* **135**, 1 (2020).
- [20] R. Govindarajan, Universal behavior of entrainment due to coherent structures in turbulent shear flow, *Phys. Rev. Lett.* **88**, 134503 (2002).
- [21] K.-I. Tanimoto, T. Kato, and K. Nakamura, Phase dynamics in SQUID's: Anomalous diffusion and irregular energy dependence of diffusion coefficients, *Phys. Rev. B* **66**, 012507 (2002).
- [22] T. Geisel, A. Zacherl, and G. Radons, Generic $\frac{1}{f}$ noise in chaotic Hamiltonian dynamics, *Phys. Rev. Lett.* **59**, 2503 (1987).
- [23] R. Guantes, J. L. Vega, and S. Miret-Artés, Chaos and anomalous diffusion of adatoms on solid surfaces, *Phys. Rev. B* **64**, 245415 (2001).
- [24] R. Guantes and S. Miret-Artés, Chaotic transport of particles in two-dimensional periodic potentials driven by ac forces, *Phys. Rev. E* **67**, 046212 (2003).
- [25] R. Klages, S. S. G. Gallegos, J. Solanpää, M. Sarvilahti, and E. Räsänen, Normal and anomalous diffusion in soft Lorentz gases, *Phys. Rev. Lett.* **122**, 064102 (2019).
- [26] K. T. McDonald, A damped oscillator as a Hamiltonian system, Joseph Henry Laboratories, Princeton University (2015), <http://kirkmcd.princeton.edu/examples/damped.pdf>.
- [27] H. Bateman, On dissipative systems and related variational principles, *Phys. Rev.* **38**, 815 (1931).
- [28] M. R. Maxey, The gravitational settling of aerosol particles in homogeneous turbulence and random flow fields, *J. Fluid Mech.* **174**, 441 (1987).
- [29] J. Bec, Multifractal concentrations of inertial particles in smooth random flows, *J. Fluid Mech.* **528**, 255 (1999).
- [30] L. Fiabane, R. Zimmermann, R. Volk, J.-F. Pinton, and M. Bourgoïn, Clustering of finite-size particles in turbulence, *Phys. Rev. E* **86**, 035301(R) (2012).
- [31] G. I. Taylor, in *The Scientific Papers of G. I. Taylor. Vol. III, Aerodynamics and the Mechanics of Projectiles and Explosions*, edited by G. K. Batchelor (Cambridge University Press, Cambridge, UK, 1958), p. 236.
- [32] L. M. Levin, Deposition of particles from a flow of aerosol onto obstacles, *Dokl. Akad. Nauk. SSSR* **91**, 1329 (1953) (in Russian).
- [33] A. V. S. Nath, A. Roy, R. Govindarajan, and S. Ravichandran, Transport of condensing droplets in Taylor-Green vortex flow in the presence of thermal noise, *Phys. Rev. E* **105**, 035101 (2022).
- [34] H. Sakaguchi, Chaotic diffusion of particles with finite mass in oscillating convection flows, *Phys. Rev. E* **65**, 067201 (2002).
- [35] W. Ott and J. A. Yorke, When Lyapunov exponents fail to exist, *Phys. Rev. E* **78**, 056203 (2008).

- [36] M. T. Maxey and S. Corrsin, Gravitational settling of aerosol particles in randomly oriented cellular flow fields, *J. Atmos. Sci.* **43**, 1112 (1986).
- [37] B. Marchetti, L. Bergougnoux, and E. Guazzelli, Falling clouds of particles in vortical flows, *J. Fluid Mech.* **908**, A30 (2021).
- [38] Y. He, S. Burov, R. Metzler, and E. Barkai, Random time-scale invariant diffusion and transport coefficients, *Phys. Rev. Lett.* **101**, 058101 (2008).
- [39] G. Benettin, L. Galgani, A. Giorgilli, and J.-M. Strelcyn, Lyapunov characteristic exponents for smooth dynamical systems and for Hamiltonian systems; a method for computing all of them. Part 1: Theory, *Meccanica* **15**, 9 (1980).
- [40] J.-P. Eckmann and D. Ruelle, Ergodic theory of chaos and strange attractors, *Rev. Modern Phys.* **57**, 617 (1985).
- [41] K. T. Alligood, T. D. Sauer, and J. A. Yorke, *Chaos: An Introduction to Dynamical Systems* (Springer-Verlag, New York, 1996), p. 379.
- [42] W. Greiner, Lyapunov exponents and chaos, in *Classical Mechanics* (Springer-Verlag, Berlin, Heidelberg, 2010), pp. 503–516.
- [43] J. Liouville, *Notesur la Théorie de la Variation des constantes arbitraires*, *J. Math. Pures Appl.* **3**, 342 (1838).
- [44] R. Majumdar, On relationships between the Lyapunov spectrum and the Morse spectrum, Iowa State University, 2001, <https://dr.lib.iastate.edu/handle/20.500.12876/77007>.
- [45] G. Baier and M. Klein, *A Chaotic Hierarchy* (World Scientific, Singapore, 1991).
- [46] M. Sandri, Numerical calculation of Lyapunov exponents, *Math. J.* **6**, 78 (1996).
- [47] J. P. Singh and B. Roy, The nature of Lyapunov exponents is (+, +, −, −). Is it a hyperchaotic system? *Chaos Solitons Fractals* **92**, 73 (2016).
- [48] D. Gupalo, A. Kaganovich, and E. Cohen, Symmetry of Lyapunov spectrum, *J. Stat. Phys.* **74**, 1145 (1994).
- [49] C. P. Dettmann and G. P. Morriss, Proof of Lyapunov exponent pairing for systems at constant kinetic energy, *Phys. Rev. E* **53**, R5545 (1996).
- [50] U. Dressler, Symmetry property of the Lyapunov spectra of a class of dissipative dynamical systems with viscous damping, *Phys. Rev. A* **38**, 2103 (1988).
- [51] J. Kaplan and J. Yorke, Functional differential equations and approximation of fixed points, *Lect. Notes Math.* **730**, 204 (1979).
- [52] H. Haken, At least one Lyapunov exponent vanishes if the trajectory of an attractor does not contain a fixed point, *Phys. Lett. A* **94**, 71 (1983).
- [53] S. Ravichandran and R. Govindarajan, Caustics and clustering in the vicinity of a vortex, *Phys. Fluids* **27**, 033305 (2015).